J. Mech. Phys. Solids 206 (2026) 106389

Contents lists available at ScienceDirect

Journal of the Mechanics and Physics of Solids

journal homepage: www.elsevier.com/locate/jmps

Contact area shrinkage and increase in wavy frictional sliding contacts

Marco Ceglie [a], Guido Violano [a], Luigi Portaluri [b,c], Luciana Algieri [b,c], Luciano Afferrante [a], Michele Scaraggi [b,c], Nicola Menga [a],*

[a] Department of Mechanics, Mathematics and Management, Politecnico di Bari, Via Orabona, 4, Bari, 70125, Italy
[b] Department of Engineering for Innovation, University of Salento, Lecce, 73100, Italy
[c] Center for Biomolecular Nanotechnologies, Istituto Italiano di Tecnologia, Arnesano, 73010, Italy

ARTICLE INFO

Keywords:
Finite strains
Contact mechanics
Friction
Contact area

ABSTRACT

The effect of material and geometric nonlinearity is often underestimated in contact mechanics. However, recent experiments reveal that classical linear models might fail to accurately predict key contact features, such as the contact area, in scenarios involving frictional sliding. In this study, we employ accurate yet simple plane-strain finite element simulations to investigate frictional sliding contact under finite elasticity. We consider both rigid and deformable sinusoidal indenters pressed against a flat substrate, exploring both periodic and aperiodic boundary conditions. Our results show that the transition of the contact area from the static conditions to the gross sliding is qualitatively governed by the pressure value. Indeed, at low pressure contact shrinkage is observed, in agreement with most experimental observations led under qualitatively similar pressure levels. Importantly, we also found a pressure threshold above which the sliding contact area can exceed the static one, especially for deformable sinusoids with high aspect ratio. To validate our numerical results, we perform ad hoc experiments with micro-fabricated soft sinusoids in either static or sliding contact against a microscope slide, which confirm the trend. Moreover, we also investigate the role of periodic boundary conditions, showing that this is not a key factor and aperiodic contacts behave almost the same. These novel findings provide deeper insights into rubber nonlinear contact mechanics at the sinusoid scale, which constitutes the building block of rough contact mechanics, showing that contact area increase is also possible without adhesion, with direct implications for real tribological systems such as tire-road and seal interactions, soft robotics locomotion, and biomechanics.

1. Introduction

Sliding frictional contacts are an integral part of everyday life, occurring across a vast range of applications, from mechanical and physical systems to biological and engineered materials (Link et al., 2020; Rosenkranz et al., 2019). They play a crucial role in locomotion (Radhakrishnan, 1998) and soft robotics (Ma et al., 2019), in the movement of joints and prosthetics (Choudhari et al., 2024), in gear mechanisms such as those of automotive transmissions (Tung and McMillan, 2004) and industrial machinery (Du et al., 2022), and in countless other fields, including electrical contacts (Toler et al., 2013), braking systems (Xiao et al., 2016), tire-road interaction (Fortunato et al., 2017) and manufacturing processes. Despite friction is frequently measured (Vakis et al., 2018) and has been studied since the time of Leonardo da Vinci (Hutchings, 2016), most theoretical approaches in contact mechanics still

---

* Corresponding author.
E-mail address: nicola.menga@poliba.it (N. Menga).

https://doi.org/10.1016/j.jmps.2025.106389
Received 14 July 2025; Received in revised form 29 September 2025; Accepted 7 October 2025

assume frictionless interfaces (Müser et al., 2017) among the other modeling approximations. This specific assumption is realistic only under small loads in dry interactions, where the real contact area remains a small fraction ($< 5 - 10\%$) of the nominal contact region (Ceglie et al., 2025b). In many cases, as for example in soft matter contacts, the contact patch is comparable in size to the dimensions of the contacting bodies (Afferrante et al., 2025), giving rise to measurable friction (Pascoe and Tabor, 1956; Yashima et al., 2015) and coupling between normal and tangential displacement (pressure) fields (Menga, 2019; Menga et al., 2021; Müller et al., 2023).

In linear elastic frictionless contact mechanics, the contact between two deformable solids can be effectively represented by modeling one body as deformable with a 'composite' elastic modulus, and the other as a rigid indenter with a composite surface topography (Barber, 2018). Remarkably, it is indifferent which body is treated as deformable, as the overall contact response remains unchanged. This approach is widely used to study both normal and sliding contacts, not only for simple geometries such as adhesive elastic spheres and cylinders (Violano and Afferrante, 2022; Violano et al., 2025; Mandriota et al., 2024) but also in more complex scenarios, including rough contacts (Greenwood and Williamson, 1966; Persson, 2006; Persson and Scaraggi, 2014; Scaraggi and Persson, 2015a,b; Afferrante et al., 2019, 2023). However, when dealing with soft materials undergoing large deformations, linear elasticity fails to accurately capture the contact mechanical response. This limitation arises from the breakdown of the small strains assumption (Lengiewicz et al., 2020). Furthermore, soft materials often exhibit a nonlinear rheological behavior, requiring constitutive models that go beyond the classical Hookean framework (Chen et al., 2010). This context highlights the need for more advanced contact models capable of accounting for nonlinear effects, to start with. These include geometric nonlinearity, associated with finite strains and displacements; material nonlinearity, arising from a nonlinear stress–strain relationships; and contact nonlinearity, influenced by friction at the interface. Nonlinear contact mechanics is a relatively recent and evolving research area. However, while significant efforts have been made to develop numerical tools for the simulation of rough contacts including nonlinearity (see, for example, Wriggers and Laursen, 2006; Al-Qudsi et al., 2022), a comprehensive understanding of how nonlinearity influences contact mechanics still requires extensive investigation.

Wang et al. (2024) numerically investigated the effect of large deformations on frictional contacts of hyperelastic materials with two dimensional surface roughness. They found that rough surfaces generally dissipate more energy than smooth ones. However, an increase in surface roughness does not necessarily lead to a higher energy dissipation rate. When the correlation length of the roughness increases or the overall rms roughness decreases beyond a certain threshold, both the real contact area and the energy dissipation rate approach those observed in smooth–smooth surface interactions.

Jiang and Liang (2024) developed an incremental model to predict the normal contact behavior of rough hyperelastic solids. In their model, the linear elastic modulus is replaced by the tangent modulus corresponding to the current stress state when calculating the contact stiffness. The relationship between the external load and the actual contact area predicted by the model showed a good agreement with finite element predictions across a wide range of contact area fractions.

Scaraggi et al. (2016) examined how both geometrical and material nonlinearities affect rubber rolling friction and the real contact area during rough sliding interactions. Their findings indicate that linear models can yield accurate friction predictions when the surface roughness exhibits moderate root mean square slope values, say ≤ 1. However, for surfaces with high root mean square slopes, nonlinear finite element simulations are necessary to accurately capture the contact area and friction behavior.

Recently, with the aid of a finite element (FE) model, some of us investigated the normal contact between a rigid sinusoidal indenter and a deformable half-plane (Ceglie et al., 2025b). The findings revealed that nonlinearity triggers frictional energy dissipation during loading–unloading indentation cycles, leading to contact hysteresis - a phenomenon typically ascribed to other interfacial effects such as adhesion, plasticity, and viscoelasticity (Li et al., 2021; Violano et al., 2021).

On the other side, three dimensional experiments on the sliding contact between a deformable hemispherical asperity and a rigid glass plate have shown that, during sliding, the contact area a decreases compared to its static value a_0 reached at the end of normal indentation (Sahli et al., 2018). A recent numerical study has shed light on this, suggesting that this trend may be driven by nonlinear effects, as confirmed by finite element simulations of three dimensional single-asperity contacts (Lengiewicz et al., 2020). However, this sliding contact behavior occurring at the single asperity level should not be scaled up to randomly rough interactions. Indeed, literature has shown that the multi-asperity description of a generic rough contact does fail in the prediction of contact mechanics, whereas the multiscale – say hierarchical overlapping of sinusoids at different wavelengths – should instead be adopted (Müser et al., 2017). It is questioned, therefore, if the sinusoid contact mechanics under finite elasticity shares the same contact area shrinkage behavior of the ball on flat geometry.

Therefore, building on the insights from Lengiewicz et al. (2020), we investigate numerically and experimentally the role of nonlinearity in the evolution of the contact area during the sliding of a two-dimensional smooth sinusoidal geometry in contact with a smooth flat substrate, under plane strain conditions. The Westergaard geometry is thus particularly well-suited for exploring the scale-dependent contact mechanics in rough interactions, as well as for applications such as the contact mechanics of human tissues and fingertips (Ayyildiz et al., 2018; Jobanputra et al., 2020). To this end, we extend the finite element model originally proposed in Ceglie et al. (2025b) to account for sliding interactions. The model incorporates both geometric and material nonlinearities, along with interfacial friction. In particular, we adopt a Coulomb–Orowan friction law at the interface, which is appropriate for rubber contacts (Chateauminois and Fretigny, 2008; Baillet and Boyer, 1995). We first explore how nonlinear effects influence contact behavior in two distinct configurations: (i) a rigid sinusoidal indenter sliding over a deformable half-plane, and (ii) a deformable sinusoidal indenter sliding over a rigid flat. For both cases, we analyze the asymmetry and evolution of the contact area throughout the sliding process. We also perform ad hoc experiments on sliding micro-fabricated wavy polymeric contacts to qualitatively corroborate the contact area numerical predictions.

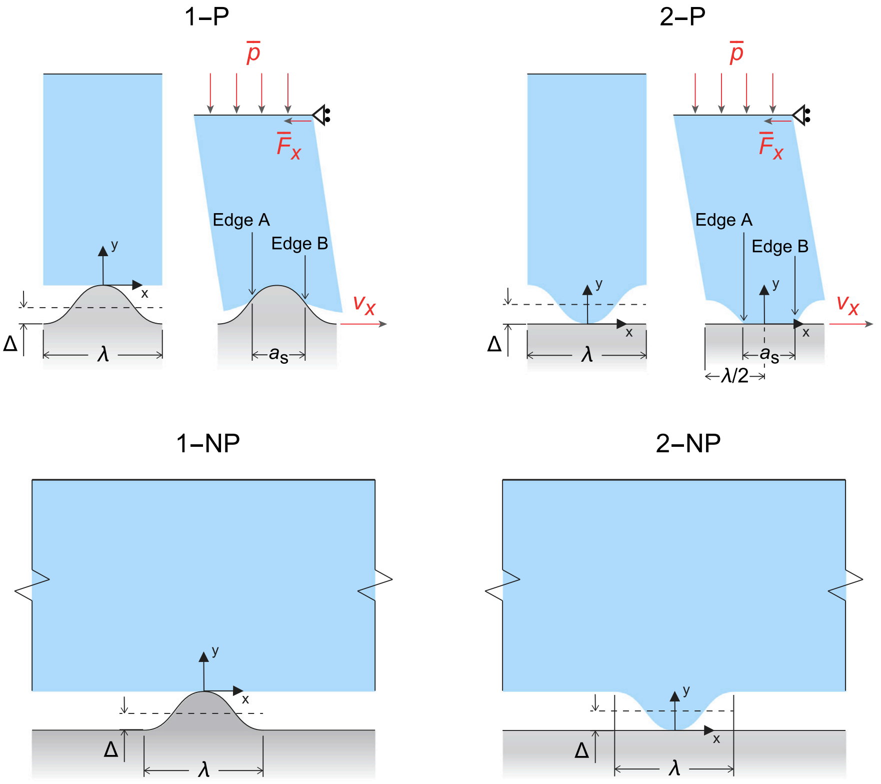

Fig. 1. Sliding contact between a deformable solid and a rigid surface. (1-P and 1-NP) Deformable flat solid is pressed against a sinusoidal rigid profile. (2-P and 2-NP) A wavy deformable solid is pressed against a rigid flat surface. Periodic (P) and aperiodic (NP) scenarios are both explored.

Our results reveal that, for high aspect ratio waviness, the variation in contact area from static to gross slip conditions depends on finite elasticity effects and, more importantly, is a pressure-dependent phenomenon. Specifically, we find that at low normal loads, the contact area decreases during sliding, an effect observed in several experiments involving 3D geometries under similar contact pressure conditions (Sahli et al., 2018; Savkoor and Briggs, 1977; Wu-Bavouzet et al., 2007). However, when the normal load exceeds a certain threshold (a regime often unexplored), the contact area can also increase during sliding. Notably, our experiments confirm this pressure-dependent behavior. Furthermore, the behavior is much more evident for the case of a deformable sinusoids against rigid flat, where nonlinearity are exacerbated. However, results are qualitatively similar for periodic and aperiodic systems, revealing the existence of a novel peculiar interface phenomenon the contact mechanics community has to deal with.

2. Numerical problem formulation

Fig. 1 illustrates the two dimensional frictional contact problem under investigation. Two bodies are pressed against each other with a mean remote pressure $\bar{p}$; the undeformed contact gap is sinusoidal, with wavelength λ and amplitude Δ. Then a relative horizontal velocity V_x is imposed, so that a transition occurs from static frictional indentation (with contact area a_0) to gross slip conditions (with contact area a_s), and a lateral (macroscopic) friction force per unit length (and transverse width) $\bar{F}_x$ opposes the relative motion. Specifically, we focus on two different contact configurations, with periodic boundary conditions (see top row in Fig. 1): in the first system (1-P), the sinusoidal profile is rigid while the flat solid (half-plane) is deformable; the second system (2-P) is reversed, with a deformable semi-infinite body with wavy shape in sliding contact with a rigid flat. For both configurations, the contact problem is also analyzed under aperiodic (NP) boundary conditions (see bottom row in Fig. 1). In this case, to minimize boundary effects, the total length of the deformable body is extended to be significantly greater than the sinusoidal wavelength λ.

Since we focus on finite elasticity, our simulations are conducted within a finite displacement framework, with contact interactions calculated in the deformed configuration. As described in Fig. 2, the reference frames in configurations 1 and 2 are centered, respectively, on the crest of the rigid sinusoid and at the midpoint of the solid surface projection on the rigid flat (i.e., at distance $\lambda/2$ from the lateral boundaries — see Fig. 1(2-P)). Furthermore, within the contact area, the deformable elements at the interface conform to the rigid counterpart, with local tangential and normal unit vectors $(\hat{\mathbf{t}}, \hat{\mathbf{n}})$. Being $(\hat{\mathbf{i}}, \hat{\mathbf{j}})$ the horizontal and vertical unit vectors, it results in

$$\begin{bmatrix} \hat{\mathbf{t}} \\ \hat{\mathbf{n}} \end{bmatrix} = \begin{bmatrix} \cos\phi & \sin\phi \\ -\sin\phi & \cos\phi \end{bmatrix} \begin{bmatrix} \hat{\mathbf{i}} \\ \hat{\mathbf{j}} \end{bmatrix} \tag{1}$$

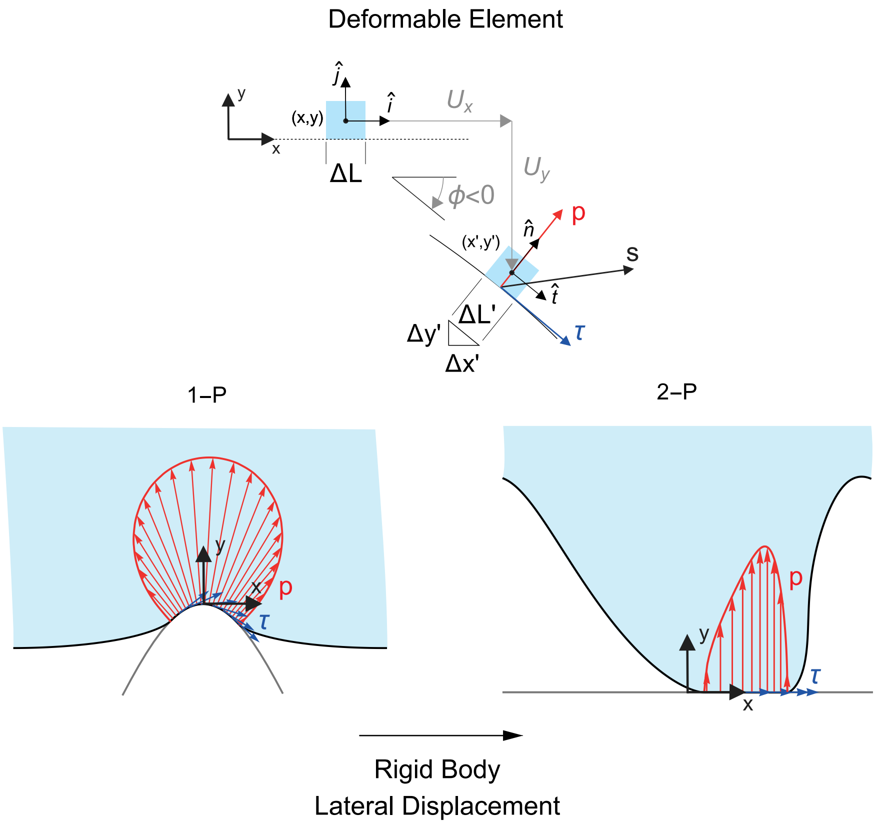

Fig. 2. Details of the nonlinear geometric framework used in the analysis. Specifically, $\mathbf{s}$ is the local Cauchy stress vector acting on the contact boundary of the solid $\mathcal{S}$ in the deformed configuration, $(\hat{\mathbf{i}}, \hat{\mathbf{j}})$ are the horizontal and vertical unit vectors in the undeformed configuration, while $(\hat{\mathbf{t}}, \hat{\mathbf{n}})$ are the local unit vectors tangent and normal to the rigid indenter surface, respectively (with local indenter slope m). In the generic deformed configuration, the interfacial element, with undeformed length ΔL, is stretched to the length $\Delta L'$, is rotated by the angle ϕ (positive if counterclockwise), and is displaced in the horizontal and vertical directions by the quantities U_{x} and U_{y}, respectively. Notably, $m = 0$ in case 2-P.

where ϕ is the local rotation of the contact element, which is assumed to be positive if counterclockwise.

Specifically, in contact configuration 1, the sinusoidal rigid indenter leads to $\tan\phi(x) = m(x) = -2\pi\Delta/\lambda \sin(2\pi x/\lambda)$, with $m(x)$ being the local slope in the contact area. Similarly, since in the contact configuration 2 the rigid substrate is horizontally flat (and $m(x) = 0$) we have that the global and local unit vectors are the same in the contact area, i.e., $(\hat{\mathbf{i}}, \hat{\mathbf{j}}) = (\hat{\mathbf{t}}, \hat{\mathbf{n}})$.

Finally, the contact Cauchy stress vector $\mathbf{s}$ can be locally decomposed into normal and tangential stresses, respectively

$$\mathbf{s} = p\hat{\mathbf{n}} + \tau\hat{\mathbf{t}} \tag{2}$$

Similarly, to simplify reading of the results in finite displacements conditions, we define the vertical s_{y} and horizontal s_{x} stresses as the projections of the stress vector $\mathbf{s}$. Hence

$$s_{\mathrm{x}}(x') = (\mathbf{s} \cdot \hat{\mathbf{i}})\sqrt{1+m^2} \quad \text{and} \quad s_{\mathrm{y}}(x') = (\mathbf{s} \cdot \hat{\mathbf{j}})\sqrt{1+m^2} \tag{3}$$

where the term $\sqrt{1+m^2} = dL'/dx'$ takes into account the increase in the local elemental length compared to the horizontal projection due to finite rotations. Note that, in the scenarios 2, $m = 0$ and $dL' \equiv dx'$. Therefore, the remote mean applied pressure $\bar{p}$ and lateral force per unit length $\bar{F}_{\mathrm{x}}$ shown in Fig. 1 are,

$$\bar{p} = \frac{1}{\lambda}\int_{-\lambda/2}^{\lambda/2} s_{\mathrm{y}}\,dx' \quad \text{and} \quad \bar{F}_{\mathrm{x}} = \frac{1}{\lambda}\int_{-\lambda/2}^{\lambda/2} s_{\mathrm{x}}\,dx' \tag{4}$$

Regarding the deformable nonlinear solid, following previous simulations on PDMS contacts (Lengiewicz et al., 2020) and even softer biological tissues (e.g., human skin) (Leyva-Mendivil et al., 2015), we assume neo-Hookean rheology. Compared to more complex models (e.g., third-order Mooney–Rivlin and second-order Ogden), the neo-Hookean solid predicts very similar stress–strain law at medium strain levels (Kim et al., 2011), such as those reported in this study (i.e., $|\varepsilon| \lessapprox 0.5$), while requiring lower computational effort. Moreover, it has also been shown to induce better agreement between the calculated and experimental contact response (Lengiewicz et al., 2020). Furthermore, since tests (Müller et al., 2019) revealed that Poisson's ratio for PDMS may vary in the range $\nu \approx 0.45 - 0.499$, we assume nearly incompressible behavior with $\nu = 0.49$, in agreement with previous calculations (Lengiewicz et al., 2020; Ceglie et al., 2025b,a), aiming at minimizing compressibility effects on our results. Indeed, we conducted a sensibility analysis showing that a further increase of ν only leads to a change in contact results of about 0.2%.

Introducing the deformation gradient tensor $\mathbf{F}$, with $J = det(\mathbf{F})$, and the right Cauchy–Green deformation tensor $\mathbf{C} = \mathbf{F}^T\mathbf{F}$, the neo-Hookean constitutive behavior in nearly incompressible solids (i.e., $\nu \approx 0.5$ and $J \approx 1$) is described by the strain energy density function (Bonet and Wood, 2008)

$$W = \frac{\mu}{2}(\bar{I}_1 - 3) + \frac{\kappa}{2}(J-1)^2, \tag{5}$$

being $\bar{I}_1 = tr(\bar{\mathbf{C}})$ the first invariant of the distortional (isochoric) right Cauchy–Green deformation tensor $\bar{\mathbf{C}} = \mathbf{C}/J^{2/3}$, and κ and μ the bulk and shear moduli,respectively. Finally, the Cauchy stress tensor is given by $\boldsymbol{\sigma} = 2/J(\mathbf{F} \cdot \frac{\partial W}{\partial \mathbf{C}} \cdot \mathbf{F}^T)$.

According to experimental findings, contact pressure has a negligible effect on frictional shear stresses in rubber contacts (Chateauminois and Fretigny, 2008; Nguyen et al., 2011); as a result, interfacial friction is conveniently implemented with a local, velocity-independent, Coulomb–Orowan law (Orowan, 1943; Baillet and Boyer, 1995), with the threshold shear stress τ_{sl} for interfacial slip given by

$$\tau_{\mathrm{sl}} = \begin{cases} \mu p, & \text{for } \mu p < \tau_{\max} \\ \tau_{\max}, & \text{for } \mu p \geq \tau_{\max} \end{cases} \tag{6}$$

where μ is the Coulomb friction coefficient, and $\tau_{\max}$ is the nominal interface shear stress.

The contact problem is analyzed using the finite element software Abaqus. To minimize boundary effects associated with finite thickness, the height of the deformable body is set to $H > 3\lambda$, a condition validated to preserve the half-plane approximation (Ceglie et al., 2025b). In the periodic configurations (1-P and 2-P in Fig. 1), displacement continuity is enforced at the lateral edges of the domain. In contrast, in the aperiodic configurations (1-NP and 2-NP in Fig. 1), the system is sufficiently extended in the horizontal direction to ensure that the contact zone remains small compared to the overall domain size. To this end, the lateral length L has been fixed so that $L > 60\lambda$.

The deformable body is discretized using plane strain elements with linear shape functions. To avoid shear locking effect, a reduced integration scheme is employed, while a hybrid formulation is adopted to account for the material's near-incompressibility. The deformable body is meshed with a finer discretization along the interface, where a mesh size of $\Delta x = \lambda/2187$ is considered. A progressively coarser mesh is employed away from the interface to optimize computational efficiency.

Normal contact is modeled using a hard contact pressure-overclosure relationship, while frictional interactions are handled via a penalty-based formulation. The normal indentation is performed under force-controlled conditions until a predefined maximum pressure is reached. More in detail, we applied a uniform pressure on the upper edge of the deformable body. Subsequently, tangential contact is investigated by applying a prescribed tangential displacement to a master node of the rigid body, which governs the displacement and forces applied to it.

To mitigate instabilities typical of nonlinear static problems, a numerical stabilization technique is employed that incorporates volume-proportional damping. The stabilization parameters are optimized through preliminary tests to ensure convergence without introducing artifacts. Specifically, an assessment of the stabilization effects, in terms of dissipated energy, shows that it remains below $10^{-7}\%$ of the internal elastic energy.

3. Materials and methods

The 2-P contact geometry has been reproduced experimentally as follows. In particular, Fig. 3A shows the fabrication protocol adopted to realize the rubber sinusoidal roughness. Two-photon polymerization (2PP) (Nanoscribe Photonic Professional GT2) is used to fabricate the IP-S resin (IP-S Photoresin - Nanoscribe GmbH & Co. KG) sinus pattern. The design consists of structures with amplitude of 25 μm and wavelength of 83 μm, over an area 6 × 6 mm^2. The Dip-In Laser Lithography (DILL) configuration is used, where a 25X objective lens is directly immersed in the liquid resin to produce polymerized structures with homogeneous printing quality (Fig. 3A-I), even for larger printing volumes, as needed in this work. In particular, the sinus pattern is fabricated on the top of a glass coated with indium-tin oxide (ITO) substrate, which provides the optical offset for the 2PP. After rinsing the IP-S sinus pattern with SU-8 developer and IPA (5 min for each solvent), a PDMS molding template is fabricated starting from the IP-S sinus replica (Fig. 3A-II). The PDMS prepolymer (Sylgard 184, Dow Corning) was mixed with the cure agent in a 20:1 mass ratio and degassed in a vacuum chamber at room temperature for 30 min. After degassing, the PDMS mixture is cast over the primary IP-S sinus mold, degassed again for 30 min, and cured for 2 h at 80 °C in the oven. Once the PDMS is cured and cooled, it was gently peeled off from the primary IP-S sinus mold, thus obtaining the negative PDMS mold (Fig. 3A-III). The PDMS mold template is thus exposed to a conformal Parylene-C deposition (Specialty Coating Systems, PDS 2010 Lab-coater), leading to the formation of an 1 μm anti-sticky layer for the subsequent sample fabrication (Fig. 3A-IV). Thus, PDMS (Sylgard 184, Dow Corning) with mixing ratio 20:1 is casted onto the ParyleneC-coated PDMS template to obtain the final sinusoidal roughness, on the top of a 150 μm substrate (Fig. 3B-V). According to Johnson and Dunn (2019), Rubino and Ioppolo (2015), a Young modulus $E \approx 1$ MPa is expected. Moreover, an optically-smooth PDMS dome (fabricated with Sylgard 184 kit, prepolymer and cross-linker with weight ratio 5:1, with the addition of 2% of Silc Pig™ Smooth-On black pigment) with radius 25.7 mm is fabricated by casting the silicon rubber onto a plano-concave lens together with the lens holder. The sinus rubber pattern is thus positioned with its geometrical center nearly the axis of symmetry of the dome, and glued on it using a PDMS drop. After curing, the typical sample realization is shown in Fig. 3C.

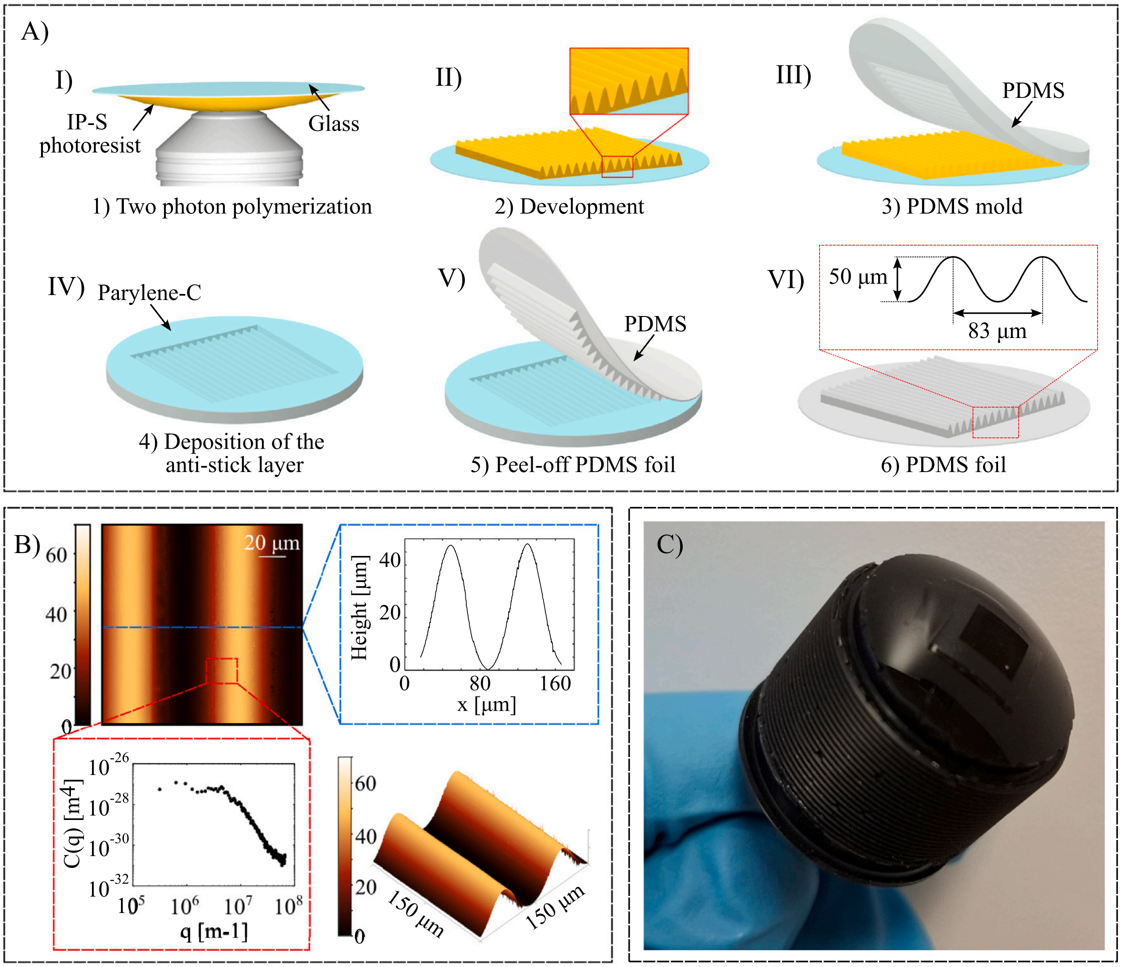

Fig. 3. (A) Rubber sinusoidal roughness fabrication process. I, 25× objective lens is immersed in the liquid resin to produce polymerized structures through two-photon polymerization. II, As-obtained polymerized structure with sinusoidal shape used as positive mold. III, Fabrication of the PDMS negative replica to be used as mold. IV, 1 μm of Parylene-C is deposited as anti-sticky layer on the PDMS mold. V, PDMS is casted into the mold to obtain the final sinusoidal roughness on the top of a 150 μm substrate. V, Design geometry of sinusoidal roughness with an amplitude of 25 μm and a wavelength of 83 μm. (B) Top-left, profilometer map of the fabricated sinusoidal roughness; Bottom-left, the magnification shows the power spectral density of the residual topography on the sinusoids, as measured with AFM; Top-right, cross section of the sinusoids profile; Bottom-right, three dimensional map of the sinusoids. (C) Optically-smooth black-colored PDMS dome with radius 25.7 mm with the sinus rubber pattern glued on the top.

The contact area is acquired with a triboscope setup configured as shown in the schematic of Fig. 4A. In particular, the contact pair is constituted by a static rubber dome (coated with the sinusoidal roughness) and a sliding microscope glass slide. The latter is cleaned with a copious amount of acetone and isopropanol and fluxed with nitrogen gas before inserting in the microscope slide holder (MLS203-1 stage from Thorlabs with a lateral resolution of 0.1 μm). The dome pin holder is constrained to a single axis load cell with 1N full scale output and resolution 1 mN. The loadcell is supported by a linear step motor with resolution 1 μm, allowing the rubber dome to be placed in contact with the microscope slide at a specific normal load. Finally, the motor is held in place by a triaxial manual micro-positioning system, which enables the dome to be finely positioned in the plane of contact. An inverted microscope (Nikon Eclipse Ti/*e*) is adopted to acquire the contact area by contrast-reflectance, returning a dark (bright) optical point acquisition in the case of contact (non-contact) spot, see Fig. 4B. In particular, Fig. 4B shows two typical (binarized) contact image acquisitions during the experiment. The rubber dome is displaced in contact with the microscope slide until a specific normal load is reached; after a settling time of 10 s, the contact image is firstly acquired at low magnification, to verify the centering of the dome with the microscope objective axis, then at high magnification to acquire contact image on a set of interacting sinusoidal structures. The latter are squeezed in contact with an average contact pressure $\approx p_{\mathrm{H}}$, where p_{H} is the maximum Hertzian pressure. Microscope sliding is thus activated with a sliding speed of 20 μm/s, allowing the specific set of sinusoidal structures to be tracked and re-centered, thanks to the manual micro-positioning system, with respect to the objective axis. Finally, the lower magnification

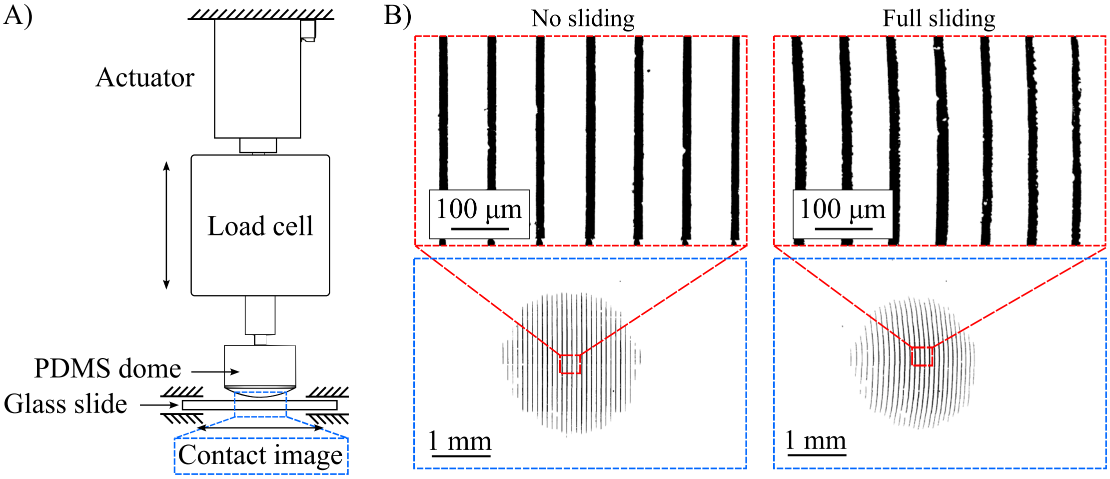

Fig. 4. Schematic of the triboscope setup for contact area measurement and related area acquisitions. (A) Triboscope setup and contact pair, constituted by a glass slide fixed to the slide holder horizontal stage. The rubber dome with sinusoidal roughness is instead connected to the load cell, the latter displaced by the actuator until a specific normal force is applied to the contact. (B) Contact images are acquired at low-magnification (blue boxed image) and high-magnification (red boxed image). In the figure, two representative contact conditions are shown, both at two different magnifications: Static contact (left), and full sliding (right).

image is acquired and the contact pair placed in a out-of-contact position. The experiment is thus repeated 3 times for each normal load. Thanks to the good optical contrast, contact area extraction is easily performed with binarization process. Specifically, within the image, pixels with high intensity values correspond to noncontact zones, while low intensity values indicate contact zones. A threshold is established at the midpoint of these two intensity values in the image, and pixels with values above this threshold are assigned the value 1, while those with lower values are assigned the value 0. As a result, the contact area is quantified as the sum of all pixels assigned the value 0.

To evaluate the frictional shear stress at the interface between PDMS used for rubber sinusoidal roughness and glass slide, a black PDMS dome was fabricated using a 20:1 weight ratio of PDMS prepolymer to cross-linker. The test was conducted under full sliding conditions at a constant sliding velocity of 20 μm/s, with the PDMS dome brought into contact with a clean glass slide. The lateral friction force (F_x) and real contact area (A_r) were measured during the test. The frictional shear stress was calculated as $\tau_{\max} = F_x/A_r \approx 0.16$ MPa, in agreement with Chateauminois and Fretigny (2008), Wei et al. (2024).

4. Calculations and results

Since in the system under investigation the deformable solid is incompressible and sufficiently thick (namely, semi-infinite), linear theory predicts that normal and tangential problems are uncoupled (Menga, 2019; Menga et al., 2021; Müller et al., 2023) and contact quantities do not vary from static to gross slip conditions, though friction occurs. Similarly, linear theory does not account for any difference between configurations 1 and 2, as only the contact gap matters in this class of contacts (Johnson, 1985; Barber, 2018). In what follows, we show that linear predictions fall short in describing real rubber behavior due to nonlinear effects (i.e., finite elasticity). These are peculiarly important in frictional sliding conditions, eventually involving contact area, stress distribution, and friction force variations compared to linear predictions.

To better highlight the role of geometric nonlinearities, in this study we consider two values of the aspect ratio of the sinusoidal roughness, namely $\Delta/\lambda = 0.1$ and $\Delta/\lambda = 0.3$. These correspond to a root mean square (rms) slope $h'_{\text{rms}} = \sqrt{2}\pi\Delta/\lambda$ of 0.44 and 1.33, respectively. The lower value is representative of the classical small-slope approximation commonly adopted in contact mechanics (Müser et al., 2017), while the higher value, although beyond the small-slope regime, is still physically relevant. Indeed, experimental measurements have reported rms slopes up to 1.2–1.3 for asphalt surfaces (Lorenz et al., 2013), and about 0.91 for human skin (Ayyildiz et al., 2018), confirming that the range investigated here is consistent with realistic surface topographies.

4.1. Normal loading

First, we analyze the behavior during purely normal indentation, in the presence of frictional interactions, expecting a certain difference between 1-P and 2-P configurations. Fig. 5a illustrates the static dimensionless contact size, a_0/λ, as a function of the dimensionless mean applied pressure $\bar{p}/E^*$ for different values of the aspect ratio Δ/λ. Westergaard's linear elastic solution is also included in the figure as a reference. Although at very low mean applied pressure both configurations recover the Westergaard linear behavior, increasing the normal load leads to different behaviors, with the 2-P configuration exhibiting overall higher values of the static contact area. As expected, this is more evident at larger aspect ratios, since these conditions boost the role of nonlinearity and

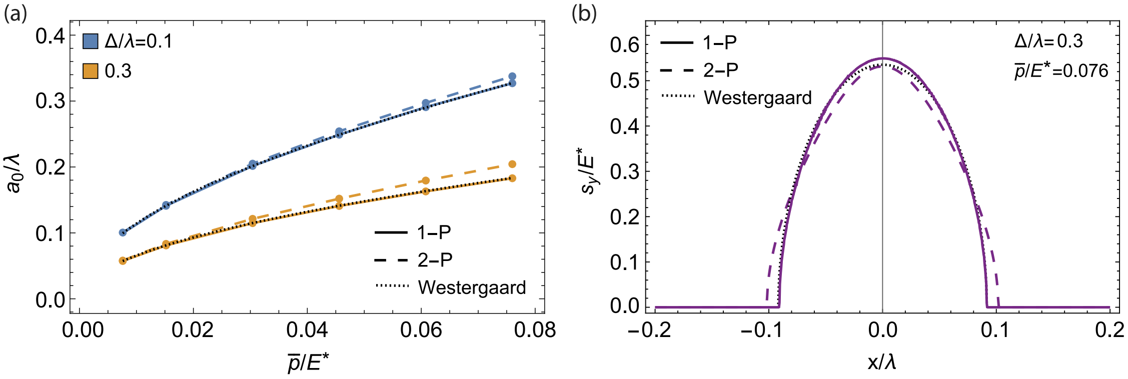

Fig. 5. (a) The static dimensionless contact size a_0/λ as a function of the dimensionless mean applied pressure $\bar{p}/E^*$ for two values of the asperity ratio Δ/λ. (b) The dimensionless vertical stress distribution s_y/E^* at the contact interface for a given value of the mean applied pressure in static contact condition. Results are given for $\tau_{\max}/E^* = 0.076$ and for both the contact model 1-P (solid line) and 2-P (dashed line). Westergaard prediction is also plotted for comparison (black dotted curve).

finite elasticity. Under these conditions, linear theory predictions cannot describe the contact behavior and, more in detail, 1-P and 2-P configurations can no longer be considered the same.

Similar differences are also evident in terms of the dimensionless vertical component of interfacial stresses s_y/E^* shown in Fig. 5b which, according to Eqs. (2)–(3), also accounts for the interfacial friction (Ceglie et al., 2025b). Indeed, we observe that results obtained for the configuration 1-P are much more in agreement with Westergaard predictions compared to those related to the 2-P configuration, with the latter being more affected by finite strains. However, as shown in Ceglie et al. (2025b), increasing the normal load, also the 1-P s_y distribution is expected to depart significantly from the Westergaard linear predictions.

4.2. Normal and tangential loading

The differences between the 1-P and 2-P configurations become much more pronounced when tangential loading is also included (in addition to normal loading), and gross sliding is achieved between the contacting solids. This is clearly shown in Fig. 6a in terms of the ratio a_s/a_0 of the contact sizes in gross slip and static conditions as a function of the mean applied pressure, for both 1-P and 2-P configurations at different aspect ratios. For the lower aspect ratio, $\Delta/\lambda = 0.1$, the gross slip contact size a_s is consistently lower than a_0. Though referring to a plane contact, this result is in agreement with several experiments (Savkoor and Briggs, 1977; Sahli et al., 2018; Wu-Bavouzet et al., 2007) showing a reduction of contact size during sliding. After some attempts to explain these results in linear theory postulating an arbitrary interaction between friction and adhesion (Johnson, 1997; Kim et al., 1998; Papangelo et al., 2019), i.e. in a debated framework also challenged theoretically (Menga et al., 2018, 2019), this behavior has recently been related to finite elasticity effects boosted by sliding interfacial friction (Lengiewicz et al., 2020).

However, our calculations also shed light on a different scenario when the aspect ratio of the sinusoidal gap is increased and, correspondingly, finite strains and displacements are further enhanced. Indeed, for $\Delta/\lambda = 0.3$, we report a pressure-dependent behavior: at low pressures, the contact size decreases in gross slip (i.e., $a_s < a_0$); however, at higher pressures, we observe an increase of the contact size during sliding. Interestingly, the latter behavior occurs for both contact configurations, though the 2-P case is quantitatively more relevant.

The von Mises stress distribution is given in Fig. 6b-e, where the deformed contact shapes in the static (black dashed) and in the gross slip regime are shown for both configurations and aspect ratios, under the same mean applied pressure $\bar{p}/E^* = 0.076$. As expected, at low aspect ratio values (see Fig. 6b,c), the 1-P and 2-P contact configurations behave qualitatively the same, as indeed suggested by the similar stress fields. More importantly, for $\Delta/\lambda = 0.3$, differences are non-negligible (see Fig. 6d,e); in fact, configuration 2-P shows higher stresses compared to 1-P and, due to friction, during sliding the deformable sinusoidal body exhibits a bending which cannot occur in 1-P, clearly leading to a different finite displacements framework between the two configurations.

The difference between 1-P and 2-P contact configurations is even more clearly shown in Fig. 7a-d, where the distribution of dimensionless vertical and horizontal components of the surface stresses s_y/E^* and s_x/E^*, respectively, are reported for each configuration. Focusing on the vertical stress distribution (see Fig. 7a-b), according to Eqs. (2)–(3), we observe that in the 1-P case s_y corresponds to the sum of the vertical components p_y and τ_y of the normal ($p\hat{\mathbf{n}}$) and tangential ($\tau\hat{\mathbf{t}}$) local stresses, respectively. For reference, the vertical stress distribution s_y at the end of the normal indentation is also shown as a black solid line (though we do not specify the quantities p_y and τ_y to simplify the reading). On the other hand, in configuration 2-P, since the deformable sinusoidal profile is flattened against the rigid horizontal surface, we have $s_y = p_y = p$. Furthermore, the rightward shift of both edges A and B in gross slip conditions compared to the static case observed in both 1-P and 2-P corresponds to different physical pictures: in the former case, the contact is asymmetric on the crest of the rigid sinusoid; in the latter, the contact interface is still flat and mainly involves the left-hand side of the deformed (bent) sinusoid. Similar arguments hold for Fig. 7c-d displaying the

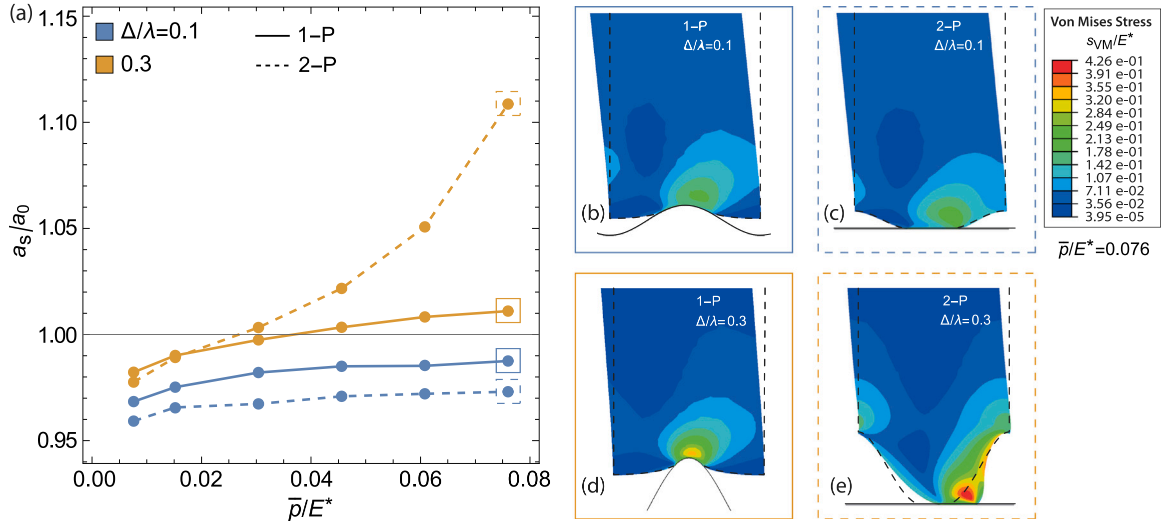

Fig. 6. (a) The gross slip contact size normalized with respect to the static contact size a_s/a_0 as a function of the dimensionless mean applied pressure $\bar{p}/E^*$. Results are given for $\tau_{max}/E^* = 0.076$, for two values of the asperity ratio Δ/λ and for both the contact model 1-P (solid line) and 2-P (dashed line). Deformed profiles and dimensionless von Mises stress fields of the deformable body in gross slip regime (b,c,d,e) for $\bar{p}/E^* = 0.076$. The static indentation deformed profiles are also superimposed for comparison (dashed black lines).

distribution of dimensionless horizontal component s_x for the two configurations. In configuration 1-P, where the sinusoid is rigid, we locally have $s_x = p_x + \tau_x$, while for the 2-P case (deformable sinusoid) $s_x = \tau_x = \tau$.

Importantly, the evolution of the dimensionless contact size a/λ for increasing values of the dimensionless frictional force $\bar{F}_x/E^*$ in the partial slip regime, i.e. during the transition from static indentation ($\bar{F}_x = 0$) to gross slip (black dots), is reported in Figs. 7e and 7d, for $\Delta/\lambda = 0.1$ and 0.3, respectively. Results are given for different values of the mean applied pressure.

As observed by Lengiewicz et al. (2020), the normal load affects both the friction force and contact size associated to gross slip conditions; yet, the points corresponding to the onset of gross sliding align on a straight line (especially at low aspect ratio — see Fig. 7e) as "a homogeneous shear stress distribution equal to the contact shear strength is suitably enforced at the onset of gross sliding". However, this argument is formally true only for 2-P case (corresponding to Lengiewicz et al. (2020) calculations), where using the second of Eqs. (4), $\bar{F}_x = \tau a_s/\lambda$ under gross sliding conditions as the local shear (tangential) stresses are horizontal.

Indeed, we observe that the contact configuration does affect the partial slip regime, due to inherent nonlinearity of the system, and the larger the aspect ratio the bigger the difference between 1-P and 2-P. Moreover, focusing on Fig. 7f corresponding to $\Delta/\lambda = 0.3$, the 1-P gross slip points are not aligned on a straight line, with the critical lateral force $\bar{F}_x$ being always larger than the corresponding 2-P value.

Although this may initially appear counterintuitive (e.g., the gross slip contact area a_s is larger for the 2-P than for the 1-P case), we recall that also the term p_x contribute to the horizontal component s_x of the interfacial stress distribution in the 1-P case and, as shown in Fig. 7c, the term p_x is not perfectly antisymmetric due to both contact area asymmetry and finite elasticity, eventually resulting in net contribution to the lateral force $\bar{F}_x$ in addition to the τ_x term. This asymmetry-induced coupling between locally normal and tangential stresses leads, for 1-P configuration, to higher values of $\bar{F}_x$ associated with gross slip conditions compared to the 2-P case. Therefore, in the nonlinear regime, the gross slip threshold must be considered configuration-dependent and, more importantly, the nonlinear local normal–tangential coupling for 1-P contact configuration highlights the importance of contact asymmetry in modulating the macroscopic frictional response, as already observed in linear theory (Menga, 2019; Menga et al., 2021; Müller et al., 2023).

4.3. Effect of the nominal shear stress

Experiments on soft matter friction suggest that the shear stress within the contact area tends to stabilize at a nearly uniform value, largely independent of the applied normal pressure (Chateauminois and Fretigny, 2008; Nguyen et al., 2011). Based on this observation, we have adopted the local (microscopic) Coulomb–Orowan friction law described in Eq. (6), where the shear stress for the interfacial slip is limited to a nominal shear stress value τ_{max}. In our experiments, in agreement with existing ones (Chateauminois and Fretigny, 2008; Wei et al., 2024; Johnson and Dunn, 2019; Rubino and Ioppolo, 2015), we have $\tau/E^* \approx 0.12$.

Moreover, also based on previous studies (Ceglie et al., 2025b), we realize that setting $\mu = 1$ in the Coulomb–Orowan friction model reduces the risk of convergence issues during FE calculations, while increasing its value negligibly affects the results. Additionally, the results are only weakly sensitive to the specific value of the friction coefficient μ. Previous analyses have shown that reducing μ by one order of magnitude leads to variations smaller than 1% in both the contact area and the frictional

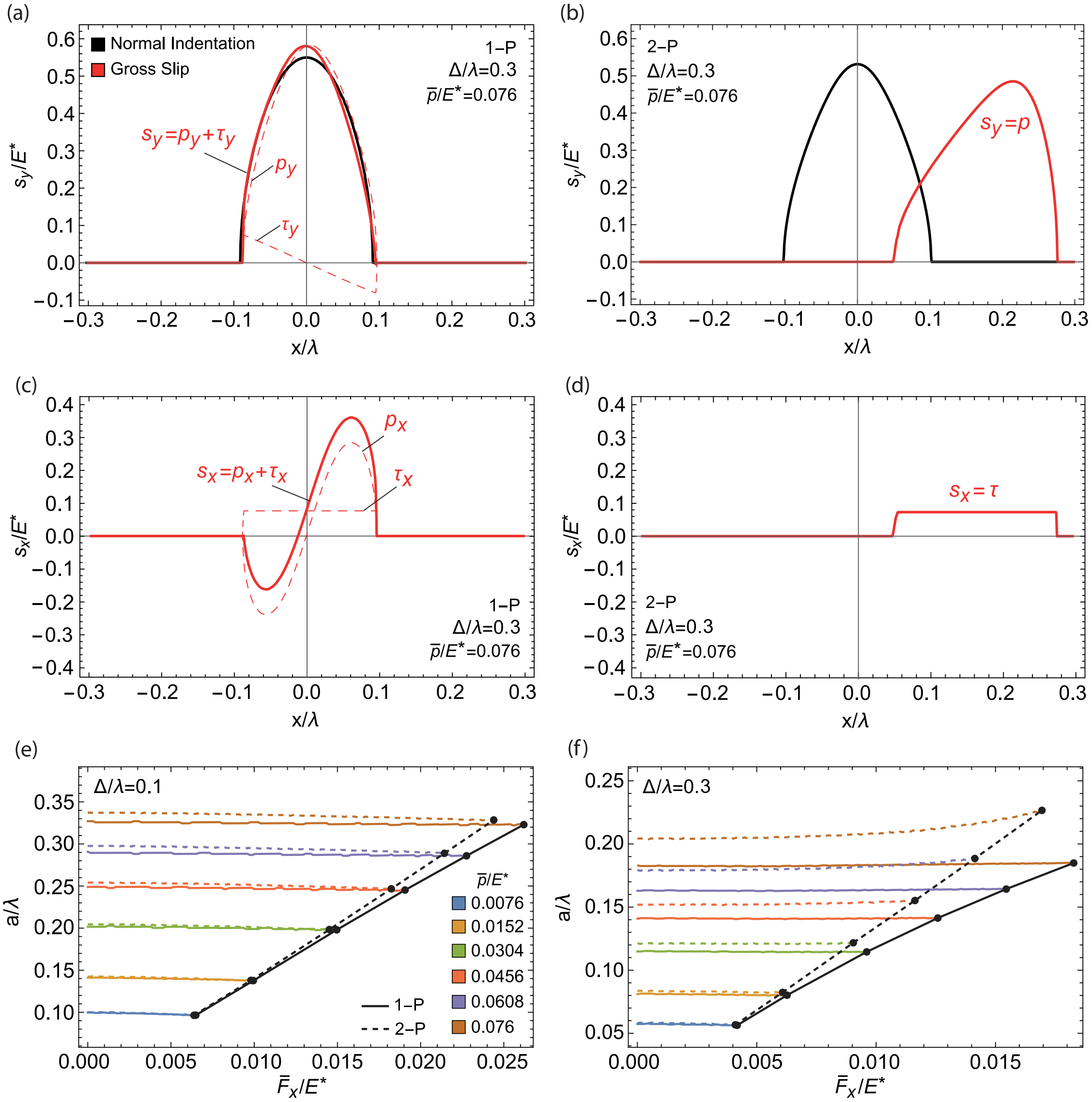

Fig. 7. The vertical stresses distribution s_y/E^* (a,b), and the horizontal stress distribution s_x/E^* (c,d) in normal indentation (black curves) and gross slip (red curves) conditions. Normal pressure and tangential shear stress contributions in the configuration 1-P are also shown (thin dashed curves). Results are given for both the configurations 1-P and 2-P with $\Delta/\lambda = 0.3$, $\bar{p}/E^* = 0.076$ and $\tau_{\max}/E^* = 0.076$. Evolution of the dimensionless contact size a/λ as a function of the dimensionless tangential force $\bar{F}_x/E^*$ during the stiction stage for different values of the mean applied pressure and for both the contact model 1-P (solid line) and 2-P (dashed line). Black points indicate the gross slip regime. Plots refer to $\Delta/\lambda = 0.1$ (e) and 0.3 (f). Results are given for $\tau_{\max}/E^* = 0.076$.

dissipation (Ceglie et al., 2025b), in agreement with the findings of Lengiewicz et al. (2020), who also reported a negligible influence of μ on the tangential contact response. Moreover, the experimental observations by Nguyen et al. (2011) also support this assumption, showing that, at the onset of gross slip, the shear stress distribution is proportional (with $\mu \approx 1$) to the normal pressure close to the contact edges and saturates at an almost constant and pressure-independent value $\tau_{\max}$ in the inner contact region.

In contrast, the threshold value $\tau_{\max}$ can significantly influence the contact response, as shown in Fig. 8, where the normalized gross slip contact size, a_s/a_0, is plotted as a function of the dimensionless nominal shear stress $\tau_{\max}/E^*$. Results are provided for different values of the mean applied pressure, $\bar{p}/E^*$ and the highest aspect ratio ($\Delta/\lambda = 0.3$). For configuration 1-P (Fig. 8a), a non-monotonic relationship between a_s/a_0 and $\tau_{\max}/E^*$ is observed. However, at high values of nominal shear stress, the gross slip contact size consistently decreases. In contrast, the pressure-dependent trend shown in Fig. 6a is confirmed for configuration 2-P (see Fig. 8b), where increasing shear stress only exacerbates the monotonic fashion of a_s/a_0. Indeed, at high normal pressures, a_s/a_0 increases with $\tau_{\max}/E^*$, while the opposite is reported at low pressures. Importantly, while the 1-P configuration is qualitatively

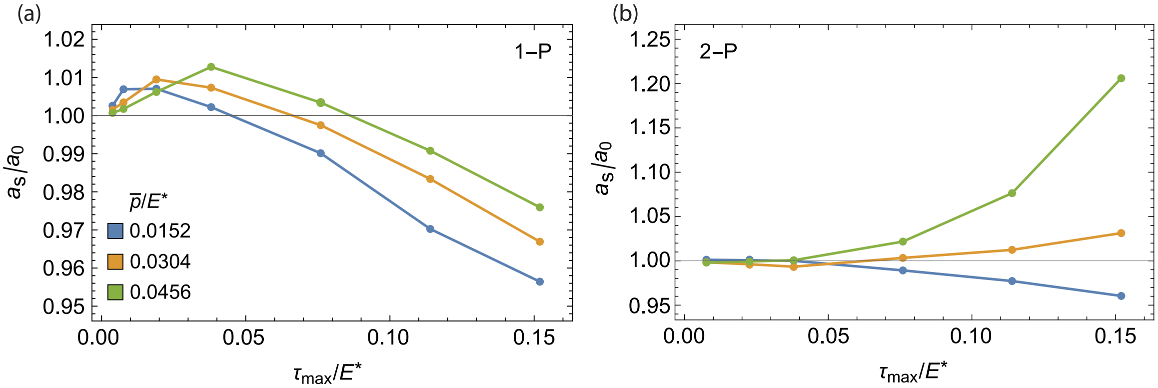

Fig. 8. The gross slip contact size normalized with respect to the static contact size a_s/a_0 as a function of the characteristic shear stress $\tau_{\max}/E^*$ for different values of the mean applied pressure $\bar{p}/E^*$. Results are given for the model 1-P (a) and 2-P (b) and for $\Delta/\lambda = 0.3$.

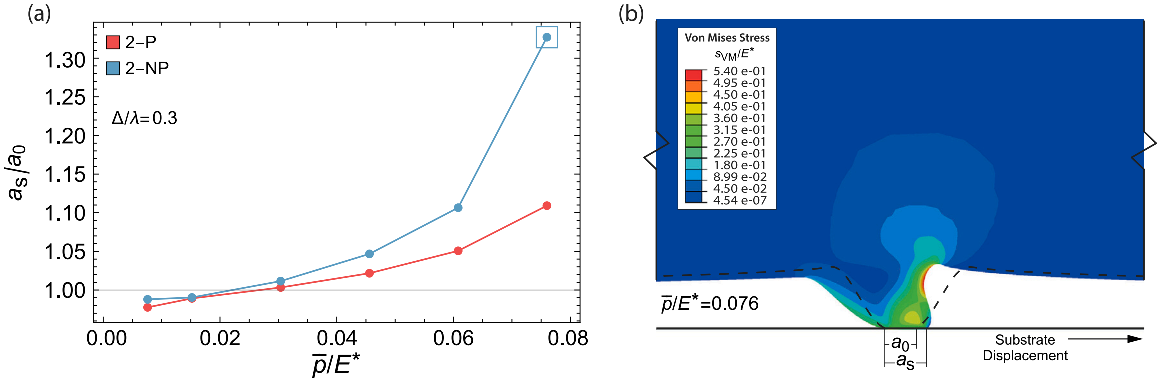

Fig. 9. (a) The gross slip contact size normalized with respect to static contact size a_s/a_0 as a function of the dimensionless applied pressure $\bar{p}/E^*$. Results are given for the configuration 2 in periodic (2-P) and aperiodic (2-NP) conditions. (b) Deformed profile and dimensionless von Mises stress field of the deformable body in gross slip regime for the configuration 2-NP at $\bar{p}/E^* = 0.076$. The static indentation deformed profile is also superimposed for comparison (dashed black lines). Result is given for $\Delta/\lambda = 0.3$ and $\tau_{\max}/E^* = 0.076$.

sensitive to the value of $\tau_{\max}/E^*$ but quantitatively poorly affected, the numerals for 2-P strongly depend on the local tangential stress value. Since the shear stresses value is a material property that is difficult to control, experimental results on 1-P configuration might be harder to interpret; therefore, we focus our tests on the 2-P, which presents smoother predictions.

4.4. Effect of boundary conditions

Periodic boundary conditions (PBCs) are commonly assumed in contact mechanics, both in numerical simulations and mathematical models, to approximate large systems by simulating only a small portion of them. However, the response of real systems may be influenced by the finite lateral size of the bodies. To determine to what extent our results are affected by the imposed PBCs, we performed an additional analysis of two configurations, referred to as 1-NP and 2-NP (see Fig. 1), in which PBCs are removed. This is equivalent to studying the contact of a single asperity with a sinusoidal shape. In the 1-NP configuration, the asperity is rigid and in contact with a deformable half-plane, whereas in the 2-NP configuration, the asperity is deformable and in contact with a flat surface. In both cases, a 2D plane strain problem is considered, similarly to the periodic scenarios. Finally, to minimize boundary effects related to the finite horizontal length L of the system, we have considered $L > 60\lambda$.

Fig. 9 shows the gross slip contact size as a function of the applied normal pressure. The results are reported for the deformable asperity case (Fig. 9b), along with the corresponding PBC configuration for comparison. Interestingly, despite some expected quantitative differences, the overall trend of a_s/a_0 with increasing pressure remains qualitatively similar. However, at higher pressures, a significantly larger increase in contact size is observed. This is clearly illustrated in Fig. 9b, where the von Mises stress distribution in the gross slip regime highlights the change in contact geometry.

For completeness, we note that in our simulations, the variation between the 1-P and 1-NP configurations in terms of a_s/a_0 remains below 1%, indicating that the two cases can be considered practically equivalent.

In general, the behavior of the 2D single-asperity system is influenced by nonlinear effects, which govern whether the contact area in gross slip decreases or increases relative to its static value, as observed in periodic systems.

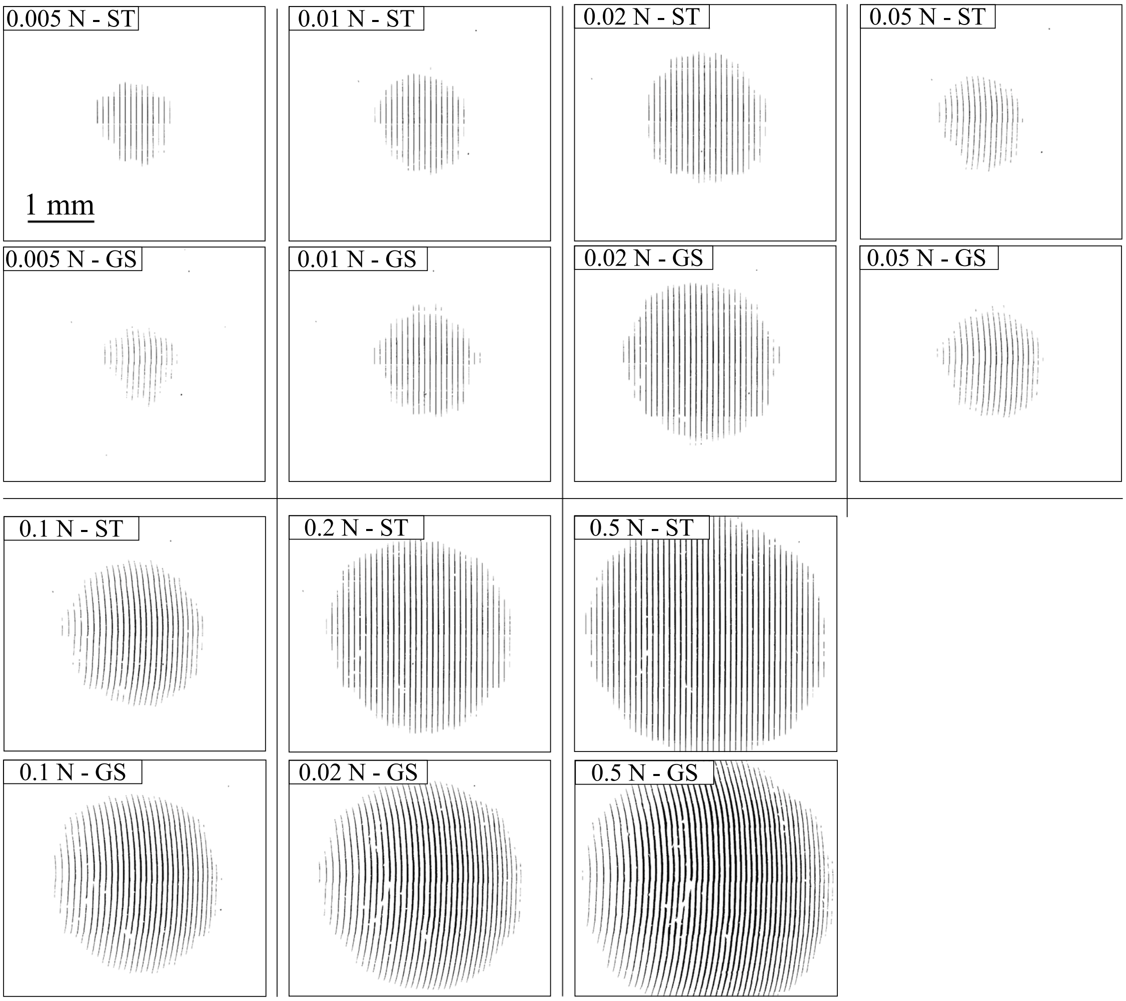

Fig. 10. Binarized contact images showing the static (top, labeled as ST) and gross slip (bottom, GS) configurations at different macroscopic normal loads F_N applied on the PDMS dome. The defects observed in the contact images are attributed to a defected fabrication, due to incomplete penetration of PDMS into the negative mold in the fabrication of the final sinusoidal roughness.

4.5. Experiments

Experimental tests have been performed, under imposed normal load, to measure the contact area corresponding to static and gross slip conditions, aiming at qualitatively validate the numerical findings discussed so far. Since calculations predict larger nonlinear effects associated with the contact configuration 2-P (deformable sinusoids against rigid flat), this is the case we focus on. Following the procedure described in Section 3, we microfabricated a PDMS foil with sinusoidal roughness, characterized by an aspect ratio equal to 0.3, and glued it to a PDMS dome, as shown in Fig. 3. The dome is squeezed in contact with a microscope glass slide, resulting into an apparent Hertzian contact (Fig. 4B, see low magnification contact images), due the relatively large separation of length scales between the apparent contact length and the fabricated sinusoid wavelength. It is noted that the adoption of a nominal point contact condition allows to avoid the several parallelism issues in the alignment of an otherwise nominally flat contact.

Apparent Hertzian contact areas have been acquired both in normal and full sliding interactions for several loads (5 mN to 0.5 N), as shown in Fig. 10. Interestingly, the apparent contact area is nearly circular regardless of the contact kinematics. This is clearly ascribable to the roughness-mediated contact, which reduces the amount of true contact area thus the tangential force (assuming the friction mostly originates from the shear stress acting in the contact areas), leading to a reduced area shrinkage (Lengiewicz et al., 2020). Therefore, whilst shrinkage may not appear at the macroscale for real applications, where non-negligible roughness is occurring most of the cases, it can affect the contact area formation at the scale of the single asperity (Sahli et al., 2018). Therefore, we have tracked the contact area evolution with applied normal load for a set of four sinusoids located near the dome axis of symmetry, thus uniformly squeezed in contact at approximately the Hertzian pressure. The normalized contact length a/λ as a

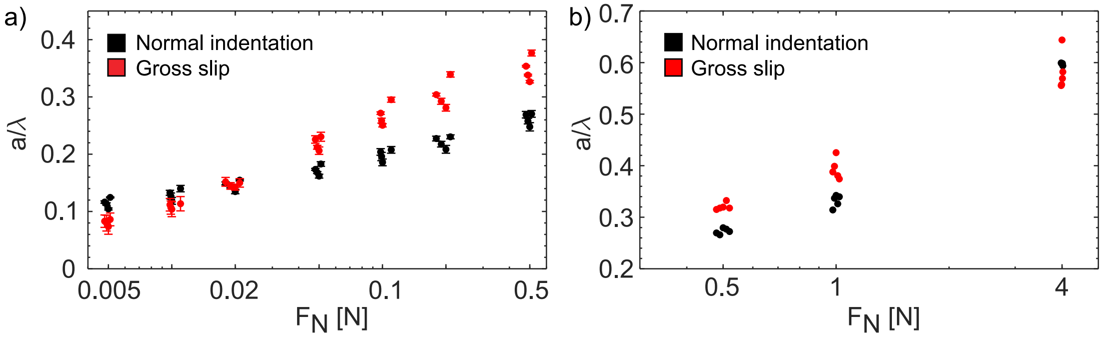

Fig. 11. Measured relative contact area a/λ, as a function of the macroscopic normal load F_N applied on the PDMS dome. Measurements refer to adjacent sinusoids (a quartet) centered with respect to the dome axis. (A) Contact area measured in static (black points) and gross slip (red) conditions, with the setup described in Section 3. (B) Contact area measured when applying a dead weight as normal force.

function of the externally applied normal load F_N is shown in Fig. 11a; in particular, a/λ is reported under static (black points) and gross slip (red) conditions, for several normal loads applied to the PDMS dome with a logarithmic step. Each cluster of points corresponds to the contact area results of the tracked sinusoids quartet, whereas the horizontal (load) shift within a quartet has been introduced only for the sake of readability. Interestingly, experiments clearly draw a crossing behavior between the normal load dependence of the contact area with and without full sliding, in agreement with the numerical findings suggested by FE calculations. Namely, with reference to the initial static contact area size, at low loads, a reduction is observed once gross sliding is kinematically imposed to the contact, as also reported by most of the existing experimental and numerical contributions on three-dimensional point contacts under similar loading conditions. Nevertheless, when increasing the normal load, gross slip conditions are associated with an increased contact size with respect to the static condition, because of friction- and aspect ratio-triggered nonlinear contact effects.

It is noted that the different sinusoids of the tracked set show slightly-different normalized contact lengths, due to the slightly-varying locally-averaged contact pressure exerted on the sinusoids as well as to microfabrication inaccuracy, however, conclusions are unaffected by this. Moreover, here the role of adhesion can be easily evaluated by recurring to the Johnson's adhesive solution to the Westergaard contact geometry (Jin et al., 2016). In particular, the impact of adhesion on contact area is given by the dimensionless adhesion number $\alpha = \sqrt{2E_\mathrm{r}\Delta\gamma\lambda^{-1}\bar{p}^{-2}}$, where E_r is the composite elastic modulus, $\Delta\gamma$ the work of adhesion, λ the sinusoid wavelength and $\bar{p}$ the pressure needed to full contact (Jin et al., 2016); for our system, assuming an adiabatic work of adhesion for the PDMS vs microscope slide interface ≈ 0.3 Jm^{-2} (Tiwari et al., 2017; Kumar et al., 2025), $\alpha \approx 0.02$, suggesting that the role of adhesion might be disregarded for our geometry at the tested normalized contact areas.

The Westergaard geometry exhibits full contact at a finite average squeezing pressure. Since this is due to the periodicity of the geometry, we expect the diverging contact area behavior between the static and full sliding condition to converge at large enough contact pressures. Nevertheless, since the adopted lead cell does not allow reaching a broader normal load coverage, we have applied larger squeezing loads on the dome with a dead weight, by adopting a relatively similar experimental setup designed for load-control experiments (not described for simplicity). In particular, Fig. 11b shows again the normalized contact area as a function of the applied normal load, but for a larger load coverage. The maximum applicable normal load is 4 N due to the triboscope design. Interestingly, at increasing normal loads the difference between the two contacting conditions does not produce any measurable difference in the contact area values. This happens at about 60% contact area in the experiments, confirming the aforementioned physical scenario.

Real applications are characterized by randomly rough interactions in most of the cases (Persson, 2006), and in most cases the roughness exhibits a broad spectrum of wavelengths (Pradhan et al., 2025). The debate on the multi-scale scenario, i.e. the description of surface roughness as a superposition (an overlapping) of sinusoids at decreasing wavelength, vs the multi-asperity scenario, i.e. the description of surface roughness as a population of differently-sized asperities distributed in the contact plane, has attracted the attention of a wide contact mechanics community in the last decade (Müser et al., 2017). However, the scientific consensus has clearly converged towards the multiscale formalism (Persson and Scaraggi, 2014; Persson, 2016; Müser et al., 2017), supporting the paradigm shift from the multi-asperity to the multi-sinusoid description of the randomly rough contact mechanics. Therefore, the scenario where contact area reduction occurs at the asperity scale in sliding rough contacts is questionable, given the multi-sinusoid nature of the contact. Most likely, either contact area reduction or increase, depending on the locally-averaged contact pressure exerted on the sinusoid at the specific magnification into the contact, is occurring. This needs to be taken into consideration in building multiscale contact mechanics formulation of rough contacts.

5. Conclusions

In this study, we investigated the influence of finite elasticity on the evolution of the contact area during sliding between sinusoidal and flat surfaces. A finite element model accounting for finite strains/displacements and interfacial friction was used to analyze the contact in two representative adhesionless configurations: (i) a rigid sinusoidal indenter against a deformable half-plane, and (ii) a deformable sinusoidal body against a rigid flat. After a purely normal indentation, we apply lateral displacement to analyze the stiction regime up to steady-state gross slip conditions. Both periodic and aperiodic boundary conditions were considered.

Our results highlight the emergence of a pressure-dependent behavior when the sinusoid aspect ratio is sufficiently high to trigger finite elasticity effects. Regardless of the contact configuration, at low pressure, gross slip conditions are associated with a reduction of the contact size, in agreement with existing three-dimensional observations. However, we also reveal the existence of the opposite behavior at relatively higher mean applied pressure values. Furthermore, in this case, the nonlinear effects play a crucial role, with the two configurations showing significant quantitative differences. Indeed, gross slip entails a larger contact area increase for the case of deformable sinusoidal solids, and larger lateral forces (i.e., macroscopic friction) for the case of rigid sinusoidal indenter. The transition from static to gross slip conditions is also accompanied by a clear asymmetry in the contact area, with distinct evolution of the contact edges.

Experiments on micro-fabricated deformable sinus pattern in static or gross sliding contact with a microscope slide have confirmed the numerical findings, highlighting excellent qualitative agreement with the theoretical scenario. It should be noted that, for high aspect ratios, our FEM simulations required stricter convergence criteria and local mesh refinement near the contact interface to avoid divergence at high contact pressures. No simulation entirely failed to converge, but the computational cost increased. This indicates that, although the numerical framework is robust, its precision at extreme loading is more sensitive to numerical settings. Furthermore, experiments allowed reaching greater mean contact pressures with respect to numerical simulations, showing that the size of static and gross slip contacts becomes again similar for contact fractions above ≈60%. Calculations also reveal that the maximum shear stress, used here as a parameter in the Coulomb–Orowan friction law, significantly influences the variation of the contact area from static to sliding conditions. Importantly, periodic boundary conditions do not qualitatively affect the observed trends.

Overall, this study confirms and stresses the importance of finite elasticity in frictional contacts. Compared to existing literature, we show that friction and surface aspect ratio can even trigger unexpected behaviors, such as the increase of the contact area, when pressure is increased, and consequently, nonlinear effects are exacerbated. This represents a new insight into contact mechanics, with relevant implications for several tribological applications involving soft materials and (relatively) sharp roughness, including tire-road and seal interactions, soft robotics, and biomechanics.

CRediT authorship contribution statement

Marco Ceglie: Writing – original draft, Visualization, Methodology, Investigation, Data curation. **Guido Violano:** Writing – review & editing, Writing – original draft, Visualization, Methodology, Investigation, Formal analysis. **Luigi Portaluri:** Writing – original draft, Visualization, Investigation, Data curation. **Luciana Algieri:** Investigation. **Luciano Afferrante:** Writing – review & editing, Supervision, Methodology, Conceptualization. **Michele Scaraggi:** Writing – review & editing, Supervision, Methodology, Funding acquisition, Conceptualization. **Nicola Menga:** Writing – review & editing, Writing – original draft, Visualization, Supervision, Project administration, Methodology, Funding acquisition, Conceptualization.

Declaration of competing interest

The authors declare that they have no known competing financial interests or personal relationships that could have appeared to influence the work reported in this paper.

Acknowledgments

This work has been partly supported by the European Union - NextGenerationEU through the Italian Ministry of University and Research under the programs (NM,MS): PRIN2022 grant nr. 2022SJ8HTC - ELectroactive gripper For mIcro-object maNipulation (ELFIN); PRIN2022 PNRR grant nr. P2022MAZHX - TRibological modellIng for sustainaBle design Of induStrial friCtiOnal inteRfacEs (TRIBOSCORE).

Data availability

Data will be made available on request.

References

Afferrante, L., Putignano, C., Menga, N., Carbone, G., 2019. Friction in rough contacts of linear viscoelastic surfaces with anisotropic statistical properties. Eur Phys J E 42 (6).

Afferrante, L., Violano, G., Carbone, G., 2023. Exploring the dynamics of viscoelastic adhesion in rough line contacts. Sci. Rep. 13 (1), 15060.

Afferrante, L., Violano, G., Demelio, G.P., 2025. Sliding viscoelastic contacts: The role of adhesion, boundary conditions, and finite geometry. Tribol. Lett. 73 (1), 5.

Al-Qudsi, A., De Lorenzis, L., Scaraggi, M., 2022. A hybrid multiscale approach for rubber contact. Front. Mech. Eng. 8, 814607.

Ayyildiz, M., Scaraggi, M., Sirin, O., Basdogan, C., Persson, B.N., 2018. Contact mechanics between the human finger and a touchscreen under electroadhesion. Proc. Natl. Acad. Sci. 115 (50), 12668–12673.

Baillet, L., Boyer, J., 1995. Comparisons of friction models for finite element modelling of closed-die forging. Contact Mech. 287–297.

Barber, J., 2018. Contact Mechanics. Springer International Publishing.

Bonet, J., Wood, R.D., 2008. Nonlinear Continuum Mechanics for Finite Element Analysis. Cambridge University Press.

Ceglie, M., Mandriota, C., Carbone, G., Menga, N., Chateauminois, A., 2025a. Anisotropic shrinkage and finite strains in confined frictional contacts. Tribol. Int. 111185.

Ceglie, M., Violano, G., Afferrante, L., Menga, N., 2025b. Finite deformations induce friction hysteresis in normal wavy contacts. Int. J. Mech. Sci. 110115.

Chateauminois, A., Fretigny, C., 2008. Local friction at a sliding interface between an elastomer and a rigid spherical probe. Eur. Phys. J. E 27, 221–227.

Chen, D.T., Wen, Q., Janmey, P.A., Crocker, J.C., Yodh, A.G., 2010. Rheology of soft materials. Annu. Rev. Condens. Matter Phys. 1 (1), 301–322.

Choudhari, A., Gupta, A.K., Kumar, A., Kumar, A., Gupta, A., Chowdhury, N., Kumar, A., 2024. Wear and friction mechanism study in knee and hip rehabilitation: A comprehensive review. Appl. Biotribology Biomed. Syst. 345–432.

Du, F., Li, D., Sa, X., Li, C., Yu, Y., Li, C., Wang, J., Wang, W., 2022. Overview of friction and wear performance of sliding bearings. Coatings 12 (9), 1303.

Fortunato, G., Ciaravola, V., Furno, A., Scaraggi, M., Lorenz, B., Persson, B.N.J., 2017. Dependency of rubber friction on normal force or load: Theory and experiment. Tire Sci. Technol. 45 (1), 25–54.

Greenwood, J.A., Williamson, J.P., 1966. Contact of nominally flat surfaces. Proc. R. Soc. Lond. Ser. A. Mathematical Phys. Sci. 295 (1442), 300–319.

Hutchings, I.M., 2016. Leonardo da Vinci's studies of friction. Wear 360, 51–66.

Jiang, C., Liang, X., 2024. An incremental contact model for hyperelastic solids with rough surfaces. Tribol. Lett. 72 (1), 1.

Jin, F., Wan, Q., Guo, X., 2016. A double-westergaard model for adhesive contact of a wavy surface. Int. J. Solids Struct. 102–103, 66–76.

Jobanputra, R., Boyle, C., Dini, D., Masen, M., 2020. Modelling the effects of age-related morphological and mechanical skin changes on the stimulation of tactile mechanoreceptors. J. Mech. Behav. Biomed. Mater. 112, 104073.

Johnson, K.L., 1985. Contact Mechanics. Cambridge University Press.

Johnson, K.L., 1997. Adhesion and friction between a smooth elastic spherical asperity and a plane surface. Proc. R. Soc. Lond. Ser. A Math. Phys. Eng. Sci. 453 (1956), 163–179.

Johnson, C.L., Dunn, A.C., 2019. Wear mode control of polydimethylsiloxane (PDMS) by load and composition. Wear 438–439, 203066.

Kim, T.K., Kim, J.K., Jeong, O.C., 2011. Measurement of nonlinear mechanical properties of PDMS elastomer. Microelectron. Eng. 88 (8), 1982–1985.

Kim, K.-S., McMeeking, R., Johnson, K., 1998. Adhesion, slip, cohesive zones and energy fluxes for elastic spheres in contact. J. Mech. Phys. Solids 46 (2), 243–266.

Kumar, S., Majhi, C., Khare, K., Singh, M.K., 2025. Adhesion study at the interface of a PDMS-elastomer and borosilicate glass-slide: effect of modulus and thickness of the elastomer. Soft Matter 21, 2493–2501.

Lengiewicz, J., de Souza, M., Lahmar, M.A., Courbon, C., Dalmas, D., Stupkiewicz, S., Scheibert, J., 2020. Finite deformations govern the anisotropic shear-induced area reduction of soft elastic contacts. J. Mech. Phys. Solids 143, 104056.

Leyva-Mendivil, M.F., Page, A., Bressloff, N.W., Limbert, G., 2015. A mechanistic insight into the mechanical role of the stratum corneum during stretching and compression of the skin. J. Mech. Behav. Biomed. Mater. 49, 197–219.

Li, L.-T., Liang, X.-M., Xing, Y.-Z., Yan, D., Wang, G.-F., 2021. Measurement of real contact area for rough metal surfaces and the distinction of contribution from elasticity and plasticity. J. Tribol. 143 (7), 071501.

Link, J.M., Salinas, E.Y., Hu, J.C., Athanasiou, K.A., 2020. The tribology of cartilage: Mechanisms, experimental techniques, and relevance to translational tissue engineering. Clin. Biomech. 79, 104880.

Lorenz, B., Persson, B., Fortunato, G., Giustiniano, M., Baldoni, F., 2013. Rubber friction for tire tread compound on road surfaces. J. Phys.: Condens. Matter. 25 (9), 095007.

Ma, S., Scaraggi, M., Yan, C., Wang, X., Gorb, S.N., Dini, D., Zhou, F., 2019. Bioinspired 3D printed locomotion devices based on anisotropic friction. Small 15 (1), 1802931.

Mandriota, C., Menga, N., Carbone, G., 2024. Enhancement of adhesion strength in viscoelastic unsteady contacts. J. Mech. Phys. Solids 192 (105826).

Menga, N., 2019. Rough frictional contact of elastic thin layers: The effect of geometrical coupling. Int. J. Solids Struct. 164, 212–220.

Menga, N., Carbone, G., Dini, D., 2018. Do uniform tangential interfacial stresses enhance adhesion? J. Mech. Phys. Solids 112, 145–156.

Menga, N., Carbone, G., Dini, D., 2019. Corrigendum to "Do uniform tangential interfacial stresses enhance adhesion?" [Journal of the Mechanics and Physics of Solids 112 (2018) 145–156]. J. Mech. Phys. Solids 133, 103744.

Menga, N., Carbone, G., Dini, D., 2021. Exploring the effect of geometric coupling on friction and energy dissipation in rough contacts of elastic and viscoelastic coatings. J. Mech. Phys. Solids 148, 104273.

Müller, C., Müser, M.H., Carbone, G., Menga, N., 2023. Significance of elastic coupling for stresses and leakage in frictional contacts. Phys. Rev. Lett. 131 (15), 156201.

Müller, A., Wapler, M.C., Wallrabe, U., 2019. A quick and accurate method to determine the Poisson's ratio and the coefficient of thermal expansion of PDMS. Soft Matter 15 (4), 779–784.

Müser, M.H., Dapp, W.B., Bugnicourt, R., Sainsot, P., Lesaffre, N., Lubrecht, T.A., Persson, B.N., Harris, K., Bennett, A., Schulze, K., et al., 2017. Meeting the contact-mechanics challenge. Tribol. Lett. 65, 1–18.

Nguyen, D.T., Paolino, P., Audry, M., Chateauminois, A., Fretigny, C., Le Chenadec, Y., Portigliatti, M., Barthel, E., 2011. Surface pressure and shear stress fields within a frictional contact on rubber. J. Adhes. 87 (3), 235–250.

Orowan, E., 1943. The calculation of roll pressure in hot and cold flat rolling. Proc. Inst. Mech. Eng. 150 (1), 140–167.

Papangelo, A., Scheibert, J., Sahli, R., Pallares, G., Ciavarella, M., 2019. Shear-induced contact area anisotropy explained by a fracture mechanics model. Phys. Rev. E 99 (5).

Pascoe, M., Tabor, D., 1956. The friction and deformation of polymers. Proc. R. Soc. Lond. Ser. A. Mathematical Phys. Sci. 235 (1201), 210–224.

Persson, B., 2006. Contact mechanics for randomly rough surfaces. Surf. Sci. Rep. 61 (4), 201–227.

Persson, B., 2016. The effect of finite roughness size and bulk thickness on the prediction of rubber friction and contact mechanics. Proc. Inst. Mech. Eng. Part C: J. Mech. Eng. Sci. 230 (9), 1398–1409.

Persson, B.N.J., Scaraggi, M., 2014. Theory of adhesion: Role of surface roughness. J. Chem. Phys. 141 (12).

Pradhan, A., Müser, M.H., Miller, N., Abdelnabe, J.P., Afferrante, L., Albertini, D., Aldave, D.A., Algieri, L., Ali, N., Almqvist, A., Amann, T., Ares, P., Balzer, B.N., Baugh, L., Berberich, E.A., Björling, M., Bobji, M.S., Bottiglione, F., Brodmann, B., Cai, W., Carbone, G., Carpick, R.W., Cassin, F., Cayer-Barrioz, J., Chowdhury, M.I., Ciavarella, M., Cihan, E., Huang, D., Delplanque, E., Deptula, A.J., Descartes, S., Dhinojwala, A., Dienwiebel, M., Dini, D., Dunn, A.C., Edwards, C., Eriten, M., Esawi, A., Espinosa-Marzal, R.M., Fang, L., Fatemi, A., Fidd, C., Gabriel, D., Gaslain, F., Giordano, G., Gómez-Herrero, J., Gontard, L., Gosvami, N.N., Greenwood, G., Greiner, C., Grejtak, T., Haroun, A., Hasan, M., Hoppe, S., Isa, L., Jackson, R.L., Jang, S., Johnson, O., Kaiser, F., Kalin, M., Kalliorinne, K., Karanjkar, P.H., Kim, S.H., Kinzelberger, S., Klapetek, P., Krick, B.A., Kumar, C., Kumar, N., Kumar, S., LaMascus, P., Larsson, R., Laux, P., Lee, M.J., Lee, P.M., Lee, W., Leriche, C., Li, J., Li, Y., Li, Y.S., Lubrecht, T.A., Lyashenko, I.A., Ma, C., Ma, T., Maaboudallah, F., Mahmood, S., Mangolini, F., Marian, M., Mazuyer, D., Meng, Y., Menga, N., Miller, T., Mulvihill, D.M., Najah, M., Nečas, D., Papadopoulos, C.I., Papangelo, A., Pauli, M., Persson, B.N.J., Peterson, A., Pitenis, A.A., Podsiadlo, P., Polajnar, M., Popov, V.L., Požar, T., Prasad, A., Prieto, G., Putignano, C., Rahman, M.H., Ramisetti, S.B., Raumel, S., Reyes, I.J., Rodriguez, N., Rodríguez Ripoll, M., Rojacz, H., Sainsot, P., Samodurova, A., Savio, D., Scaraggi, M., Schaefer, F., Scherrer, S.W., Schulze, K.D., Shaffer, K.E., Sidebottom, M.A., Skaltsas, D., Soni, J., Spies, C., Stachowiak, G.W., Steinhoff, L., Strandwitz, N.C., Sun, K., Tripathi, S., Tuckart, W.R., Ugar, S., Valtr, M., Van Meter, K.E., Vdovak, J., Vilhena, J.G., Violano, G., Vorlaufer, G., Walczak, M., Weber, B., Woloszynski, T., Wolski, M., Yadav, A., Yastrebov, V.A., Yongjian, M., Yuan, L., Yus, J., Zhang, J., Zhang, X., Zheng, Q., Pastewka, L., Jacobs, T.D.B., 2025. The surface-topography challenge: A multi-laboratory benchmark study to advance the characterization of topography. Tribol. Lett. 73 (3).

Radhakrishnan, V., 1998. Locomotion: dealing with friction. Proc. Natl. Acad. Sci. 95 (10), 5448–5455.

Rosenkranz, A., Grützmacher, P.G., Gachot, C., Costa, H.L., 2019. Surface texturing in machine elements- a critical discussion for rolling and sliding contacts. Adv. Eng. Mater. 21 (8), 1900194.

Rubino, E., Ioppolo, T., 2015. Young's modulus and loss tangent measurement of polydimethylsiloxane using an optical lever. J. Polym. Sci. Part B: Polym. Phys. 54 (7), 747–751.

Sahli, R., Pallares, G., Ducottet, C., Ben Ali, I., Al Akhrass, S., Guibert, M., Scheibert, J., 2018. Evolution of real contact area under shear and the value of static friction of soft materials. Proc. Natl. Acad. Sci. 115 (3), 471–476.

Savkoor, A.R., Briggs, G.A.D., 1977. The effect of tangential force on the contact of elastic solids in adhesion. Proc. R. Soc. Lond. 356 (1684), 103–114.

Scaraggi, M., Comingio, D., Al-Qudsi, A., De Lorenzis, L., 2016. The influence of geometrical and rheological non-linearity on the calculation of rubber friction. Tribol. Int. 101, 402–413.

Scaraggi, M., Persson, B.N.J., 2015a. Friction and universal contact area law for randomly rough viscoelastic contacts. J. Phys.: Condens. Matter. 27 (10), 105102.

Scaraggi, M., Persson, B.N.J., 2015b. General contact mechanics theory for randomly rough surfaces with application to rubber friction. J. Chem. Phys. 143 (22).

Tiwari, A., Dorogin, L., Bennett, A., Schulze, K., Sawyer, W., Tahir, M., Heinrich, G., Persson, B., 2017. The effect of surface roughness and viscoelasticity on rubber adhesion. Soft Matter 13 (19), 3602–3621.

Toler, B.F., Coutu, R.A., McBride, J.W., 2013. A review of micro-contact physics for microelectromechanical systems (MEMS) metal contact switches. J. Micromech. Microeng. 23 (10), 103001.

Tung, S.C., McMillan, M.L., 2004. Automotive tribology overview of current advances and challenges for the future. Tribol. Int. 37 (7), 517–536.

Vakis, A.I., Yastrebov, V.A., Scheibert, J., Nicola, L., Dini, D., Minfray, C., Almqvist, A., Paggi, M., Lee, S., Limbert, G., et al., 2018. Modeling and simulation in tribology across scales: An overview. Tribol. Int. 125, 169–199.

Violano, G., Afferrante, L., 2022. On the long and short-range adhesive interactions in viscoelastic contacts. Tribol. Lett. 70 (3), 68.

Violano, G., Chateauminois, A., Afferrante, L., 2021. Rate-dependent adhesion of viscoelastic contacts, Part I: Contact area and contact line velocity within model randomly rough surfaces. Mech. Mater. 160, 103926.

Violano, G., Demelio, G.P., Afferrante, L., 2025. Sliding viscoelastic contacts: Reciprocating adhesive contact mechanics and hysteretic loss. Tribol. Lett. 73 (1), 21.

Wang, C., Li, Y., Li, Y., Fan, Y., Feng, Z., 2024. Coupling effect of large deformation and surface roughness on dynamic frictional contact behaviors of hyperelastic material. Comput. Mech. 1–19.

Wei, H., Wang, Z., Tu, X., Cheng, X., Li, L., Wang, S., Li, C., 2024. Does static friction information predict the onset of sliding for soft material? Int. J. Solids Struct. 305, 113087.

Wriggers, P., Laursen, T.A., 2006. Computational Contact Mechanics, vol. 2, Springer.

Wu-Bavouzet, F., Clain-Burckbuchler, J., Buguin, A., De Gennes, P., Brochard-Wyart, F., 2007. Stick-slip: Wet versus dry. J. Adhes. 83 (8), 761–784.

Xiao, X., Yin, Y., Bao, J., Lu, L., Feng, X., 2016. Review on the friction and wear of brake materials. Adv. Mech. Eng. 8 (5), 1687814016647300.

Yashima, S., Romero, V., Wandersman, E., Frétigny, C., Chaudhury, M., Chateauminois, A., Prevost, A., 2015. Normal contact and friction of rubber with model randomly rough surfaces. Soft Matter 11 (5), 871–881.